Research Article | Vol. 26, No. 10 | 14 May 2018 | OPTICS EXPRESS 12415
Optics EXPRESS

Coherent illumination spectroscopy of nanostructures and thin films on thick substrates

FEI HE,[1] KEVIN F. MACDONALD,[2] AND XU FANG[1,*]

[1]School of Electronics and Computer Science, University of Southampton, SO17 1BJ, UK
[2]Optoelectronics Research Centre and Centre for Photonic Metamaterials, University of Southampton, SO17 1BJ, UK
*x.fang@soton.ac.uk

Abstract: Many nanophotonic and nanoelectronic devices contain nanostructures and ultrathin films on the surface of a thick, effectively semi-infinite, substrate. Here we consider a spectroscopic technique based upon coherent illumination, for characterising such samples. The method uses two counter-propagating light beams to generate specific field configurations at the substrate surface plane, which can be modulated, for example, to selectively excite and thereby discriminate between resonant modes of plasmonic nanostructures, or to measure thin films thickness with nanometre resolution. The technique offers a variety of practical applications for the coherent illumination in solid state physics, analytical chemistry, biochemistry, and nano-engineering.

OCIS codes: (250.5403) Plasmonics; (160.3918) Metamaterials; (310.6628) Subwavelength structures, nanostructures; (030.1670) Coherent optical effects; (240.6490) Spectroscopy, surface; (310.6860) Thin films, optical properties.

References and links

1. L. F. Chen, C. K. Ong, C. P. Neo, V. V. Varadan, and V. K. Varadan, *Microwave electronics: measurement and materials characterization* (Wiley, 2007).
2. M. Brustolon and E. Giamello, *Electron paramagnetic resonance: a practitioner's toolkit* (Wiley, 2009).
3. K. D. Heylman, N. Thakkar, E. H. Horak, S. C. Quillin, C. Cherqui, K. A. Knapper, D. J. Masiello, and R. H. Goldsmith, "Optical microresonators as single-particle absorption spectrometers," Nat. Photonics **10**(12), 788–795 (2016).
4. R. Engeln, G. Berden, R. Peeters, and G. Meijer, "Cavity enhanced absorption and cavity enhanced magnetic rotation spectroscopy," Rev. Sci. Instrum. **69**(11), 3763–3769 (1998).
5. J. Hu, "Ultra-sensitive chemical vapor detection using micro-cavity photothermal spectroscopy," Opt. Express **18**(21), 22174–22186 (2010).
6. G. Berden, R. Peeters, and G. Meijer, "Cavity ring-down spectroscopy: Experimental schemes and applications," Int. Rev. Phys. Chem. **19**(4), 565–607 (2000).
7. S. Rosenblum, Y. Lovsky, L. Arazi, F. Vollmer, and B. Dayan, "Cavity ring-up spectroscopy for ultrafast sensing with optical microresonators," Nat. Commun. **6**(1), 6788 (2015).
8. E. Plum, K. F. MacDonald, X. Fang, D. Faccio, and N. I. Zheludev, "Controlling the optical response of 2D matter in standing waves," ACS Photonics **4**(12), 3000–3011 (2017).
9. D. G. Baranov, A. Krasnok, T. Shegai, A. Alù, and Y. Chong, "Coherent perfect absorbers: linear control of light with light," Natl. Rev. **2**, 17064 (2017).
10. N. Yang and A. E. Cohen, "Local geometry of electromagnetic fields and its role in molecular multipole transitions," J. Phys. Chem. B **115**(18), 5304–5311 (2011).
11. X. Fang, K. F. MacDonald, E. Plum, and N. I. Zheludev, "Coherent control of light-matter interactions in polarization standing waves," Sci. Rep. **6**(1), 31141 (2016).
12. X. Fang, M. L. Tseng, D. P. Tsai, and N. I. Zheludev, "Coherent excitation-selective spectroscopy of multipole resonances," Phys. Rev. Appl. **5**(1), 014010 (2016).
13. P. Woźniak, P. Banzer, and G. Leuchs, "Selective switching of individual multipole resonances in single dielectric nanoparticles," Laser Photonics Rev. **9**(2), 231–240 (2015).
14. S. W. Hell, "Toward fluorescence nanoscopy," Nat. Biotechnol. **21**(11), 1347–1355 (2003).
15. M. L. Tseng, X. Fang, V. Savinov, P. C. Wu, J. Y. Ou, N. I. Zheludev, and D. P. Tsai, "Coherent selection of invisible high-order electromagnetic excitations," Sci. Rep. **7**, 44488 (2017).

#320164 https://doi.org/10.1364/OE.26.012415
Journal © 2018 Received 23 Feb 2018; revised 23 Mar 2018; accepted 6 Apr 2018; published 1 May 2018

Optics EXPRESS

16. G. Bauer and W. Richter, *Optical characterization of epitaxial semiconductor layers* (Springer, 1996).
17. H. G. Tompkins and W. A. McGahan, *Spectroscopic ellipsometry and reflectometry: a user's guide* (Wiley, 1999).
18. Y. Y. Wang, R. X. Gao, Z. H. Ni, H. He, S. P. Guo, H. P. Yang, C. X. Cong, and T. Yu, "Thickness identification of two-dimensional materials by optical imaging," Nanotechnology **23**(49), 495713 (2012).
19. H. Zhang, F. Ran, X. Shi, X. Fang, S. Wu, Y. Liu, X. Zheng, P. Yang, Y. Liu, L. Wang, X. Huang, H. Li, and W. Huang, "Optical thickness identification of transition metal dichalcogenide nanosheets on transparent substrates," Nanotechnology **28**(16), 164001 (2017).
20. S. M. Hein and H. Giessen, "Tailoring magnetic dipole emission with plasmonic split-ring resonators," Phys. Rev. Lett. **111**(2), 026803 (2013).
21. M. Kasperczyk, S. Person, D. Ananias, L. D. Carlos, and L. Novotny, "Excitation of magnetic dipole transitions at optical frequencies," Phys. Rev. Lett. **114**(16), 163903 (2015).
22. P. B. Johnson and R. W. Christy, "Optical constants of the noble metals," Phys. Rev. B **6**(12), 4370–4379 (1972).
23. Z. Liu, A. Boltasseva, R. H. Pedersen, R. Bakker, A. V. Kildishev, V. P. Drachev, and V. M. Shalaev, "Plasmonic nanoantenna arrays for the visible," Metamaterials (Amst.) **2**(1), 45–51 (2008).
24. X. Fang, K. F. MacDonald, and N. I. Zheludev, "Controlling light with light using coherent metadevices: all-optical transistor, summator and invertor," Light Sci. Appl. **4**(5), e292 (2015).
25. S. Thongrattanasiri, F. H. L. Koppens, and F. J. García de Abajo, "Complete optical absorption in periodically patterned graphene," Phys. Rev. Lett. **108**(4), 047401 (2012).
26. Z. Yin and F. W. Smith, "Optical dielectric function and infrared absorption of hydrogenated amorphous silicon nitride films: experimental results and effective-medium-approximation analysis," Phys. Rev. B Condens. Matter **42**(6), 3666–3675 (1990).
27. W. Cai, U. K. Chettiar, H. K. Yuan, V. C. de Silva, A. V. Kildishev, V. P. Drachev, and V. M. Shalaev, "Metamagnetics with rainbow colors," Opt. Express **15**(6), 3333–3341 (2007).
28. C. Bohling and W. Sigmund, "Self-limitation of native oxides explained," Silicon **8**(3), 339–343 (2016).
29. E. D. Palik, *Handbook of Optical Constants of Solids* (Academic, 1985).
30. X. Fang, M. L. Tseng, J. Y. Ou, K. F. MacDonald, D. P. Tsai, and N. I. Zheludev, "Ultrafast all-optical switching via coherent modulation of metamaterial absorption," Appl. Phys. Lett. **104**(14), 141102 (2014).

1. Introduction

The optical properties of subwavelength-thickness materials can manifest differently in travelling wave and standing wave electromagnetic fields, presenting a variety of opportunities, not least in spectroscopic applications. For example, in the microwave regime, standing waves are used to measure material dielectric permittivity and magnetic permeability [1], and to suppress background noise in electron paramagnetic resonance spectroscopy [2]. In the infrared to visible range, they are harnessed in absorption [3], magnetic rotation [4], photothermal [5], and cavity ring-down/up spectroscopies [6, 7]. In all of these cases, the standing waves are formed inside a cavity illuminated by a single input travelling wave. Recent works have shown that standing waves formed in free space by the interference of two coherent input light beams can be engaged to coherently control all manner of light-matter interactions in thin film (meta)materials [8, 9], from absorption to four-wave mixing, at femtosecond time scales and at arbitrarily low intensities (even at the single photon level). For spectroscopic applications, this 'four-port' (two input, two output beam) configuration removes the constraint on operational wavelength range imposed by a geometrically fixed cavity, and provides access to a variety of field configurations that are only achievable with two input beams of independently controllable intensity and polarization [10, 11].

The principle of coherent 'excitation-selective' spectroscopy was first introduced and experimentally demonstrated in application to plasmonic nano-antennas supported on ultrathin (i.e. subwavelength thickness) membrane substrates [12]. Rather than spatially structuring a travelling light wave [13], the technique utilizes an illumination configuration similar to that in 4Pi confocal and widefield I^5M microscopy [14] to create specific electromagnetic field distributions. Recent computational analyses have illustrated that the technique may be harnessed to detect and discriminate among weak, high-order (quadrupole, octupole, toroidal) modes in free-standing, ultra-thin plasmonic metasurfaces [15]. The subwavelength thickness of target (analyte) structures and materials is essential to the coherent excitation paradigm, but that of any substrate is not. The use of ultra-thin membrane substrates in a majority of experimental works on coherent control [8, 9] is a convenience

Optics EXPRESS

rather than a fundamental requirement, in that they represent only a small perturbation to the ideal directional symmetry of the four-port arrangement.

Here we consider the application of coherent 'excitation-selective' spectroscopy techniques in a more technologically-typical configuration where analytes are supported on optically thick, i.e. semi-infinite, substrates that break the directional symmetry of the system. We analyze the selective coherent (standing wave) excitation of electric and magnetic resonant modes in plasmonic nanostructures on a bulk glass substrate, and further show that coherent illumination spectroscopy may be applied to the detection and interrogation of homogenous thin-films. Such films, with thickness ranging from less than a nanometre to several tens of nanometres (e.g. native oxide on silicon, gate dielectrics in logic devices, and two-dimensional materials) play a key part in nanophotonics and nanoelectronics. Non-destructively detecting their (possibly unwanted) presence and/or accurately determining their thickness is an extremely important and non-trivial challenge. In this regard, coherent illumination spectroscopy can complement the existing toolkit of optical techniques (which includes spectroscopic ellipsometry, reflectometry, white-light interferometry and contrast imaging [16–19]), providing an option that is particularly suited to the characterization of absorptive thin films on the surface of transparent bulk substrates.

2. Optical standing waves inside and outside a substrate

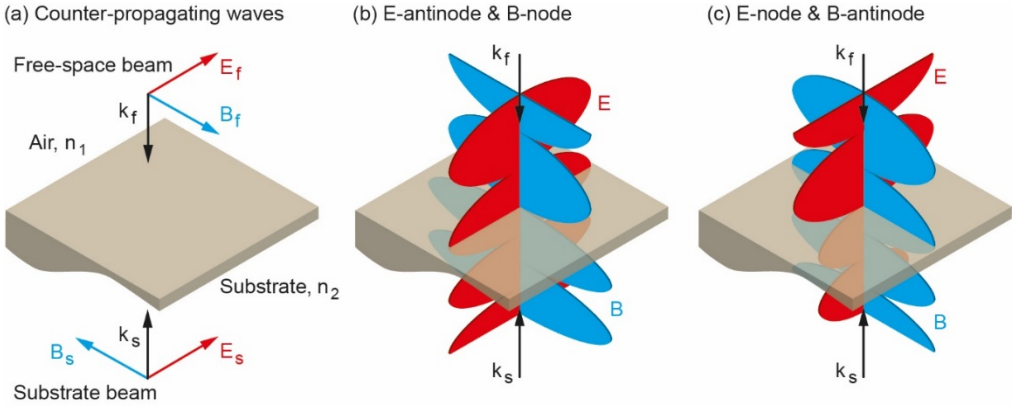

Fig. 1. Coherent illumination of a substrate surface plane using two counter-propagating light beams. Schematic illustrations of: (a) Wave- and electric/magnetic field vector directions for the two collinearly polarized incident beams, relative to the interface between air [refractive index n_1] and a semi-infinite substrate of refractive index n_2. (b, c) Electric and magnetic field distributions for standing waves in which the surface of the substrate is (b) at an electric field antinode [E-antinode] and magnetic field node [B-node]; (c) at an electric field node [E-node] and magnetic field antinode [B-antinode].

We first consider coherent illumination for a thick transparent substrate without any analyte at the surface (Fig. 1). A pair of counter-propagating, mutually coherent light beams are utilized - one normally incident on the surface in air (i.e. the free-space beam), the other in the substrate (i.e. substrate beam) (Fig. 1(a)). These two beams have the same frequency and linear polarisation but may be different in phase and amplitude. With appropriate selection of their relative phase and amplitude, the two incident waves can form a standing wave in both air and the substrate (Figs. 1(b) and 1(c)). Such configurations can be understood starting from the electromagnetic fields at the substrate surface. The electric field E and magnetic field B at this position are:

$$E = \frac{2n_1}{n_1 + n_2} E_f + \frac{2n_2}{n_1 + n_2} E_s \qquad (1)$$

Optics EXPRESS

$$B = \frac{2n_2}{n_1 + n_2} B_f + \frac{2n_1}{n_1 + n_2} B_s \tag{2}$$

where n_1 and n_2 are the refractive indices of air and the substrate, respectively. E_f and E_s are the electric fields of the free-space and the substrate beams, respectively, and B_f and B_s the corresponding magnetic fields. When $B = 0$, the corresponding Poynting vector indicates that the net power flow across the air-substrate interface is zero: a standing wave is established in the whole space. The corresponding surface electric field is very strong; it is in fact the largest surface electric field achievable for a given total input power, regardless of whether this power is contained within one incident beam or distributed between two incident beams. Figure 1(b) illustrates the field configuration near the interface. The standing wave has two distinctive sections in air and in the substrate due to their different refractive indices. The air-substrate interface is at the E-antinode (electric field antinode) and B-node (magnetic field node) of the standing wave. Figure 1(c) shows the field configuration when $E = 0$, i.e. with the interface at the E-node and B-antinode. The field configuration is characteristically similar to that in Fig. 1(b) in that: a standing wave is formed in air and the substrate with zero net power flow across the interface; and the interface magnetic field is the maximal value achievable for a given total input power. Importantly, due to the difference between n_1 and n_2, switching between the two configurations shown in Figs. 1(b) and 1(c) is only achieved if both the relative phase and amplitude of the two incident beams are changed.

If nanoscale analytes are placed on the surface of the substrate, they will be excited by the surface fields described by Eqs. (1) and (2). The light-matter interactions may present differently between the two standing wave (i.e. two beam coherent) illumination configurations and between standing wave and single beam (travelling wave) illumination modes; and can be readily switched among these regimes by changing the relative phase and/or intensity of the two incident beams. In what follows, by numerically simulating the optical absorption of a selection of samples, we demonstrate possible applications to the selective excitation of (discrimination between) plasmonic resonances and to measurement of thin film thickness.

3. Selective excitation of multipole resonances in nanostructures

The interaction between a nanoscale object and the surface electromagnetic field can be expressed as the multipolar Hamiltonian of $-p \cdot E - m \cdot B - [Q\nabla] \cdot E - \cdots$, where p, m and Q are the electric dipole moment, magnetic dipole moment and electric quadrupole moment, respectively [20, 21]. For the purposes of the present proof-of-principle demonstration, only the two leading terms, the electric dipole interaction $p \cdot E$ and the magnetic dipole interaction $m \cdot B$, are considered.

Figure 2 illustrates control over $p \cdot E$ using the example of a planar plasmonic metamaterial. The metamaterial is an array of gold nanorods on top of an infinitely thick glass substrate (Fig. 2(a)). Each rod is 270 nm in length, 50 nm in width and 30 nm in height. The array is assumed to be infinitely large in the xy plane, with a periodicity of 400 nm in both directions. Figure 2(b) compares the spectral dispersion of the metamaterial's absorption under three modes of illumination by: (1) a single, travelling light wave impinging from the air (i.e. the free-space beam only); (2) a standing wave formed by two counter-propagating light beams, with the sample at the E-antinode (i.e. B-node); (3) a standing wave with the sample at the E-node (i.e. B-antinode). The absorption is normalized against the total input power for each case. These spectra are calculated using a 3D finite-element Maxwell solver (COMSOL Multiphysics), with the complex permittivity of gold described by the Drude model [22, 23]. The glass substrate is taken to be infinitely thick with a real refractive index of 1.5, and all beams to be polarized in the y direction. For the standing wave excitation modes, the E fields of the two incident waves are either in phase or π out of phase in the xy plane bisecting the nanorods.

Optics EXPRESS

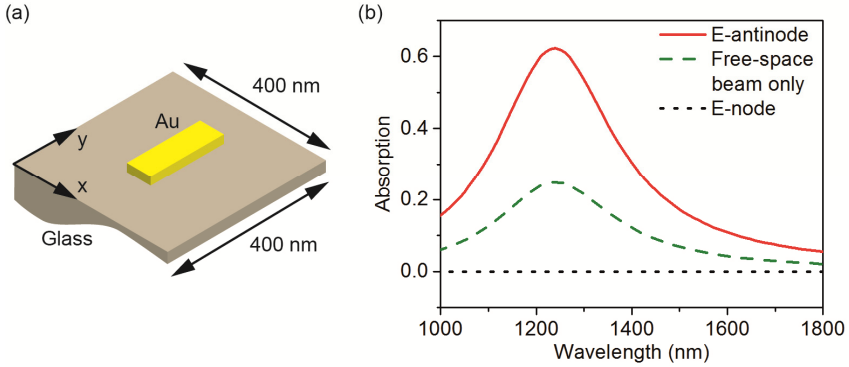

Fig. 2. Coherent excitation of an electric dipolar resonant mode in a plasmonic metamaterial. (a) Schematic of a unit cell of the metamaterial comprising a gold nanorod on an infinitely thick glass substrate. The periodicity of the array is 400 nm in both *x* and *y* directions. The nanorod is 270 nm long, 50 nm wide and 30 nm in thickness. (b) Spectral dispersion of metasurface absorption for coherent illumination modes locating the nanorod at a standing wave E-antinode [red line] or E-node [black], and for single beam [travelling wave] illumination from the free space side. In all cases, light is polarized in the *y* direction, parallel to the long axis of the nanorods.

Under single beam, travelling wave illumination the nanorods present a broad absorption peak with the center wavelength at 1240 nm and the maximum value of 0.25 (Fig. 2(b)) – a resonant response that can be approximated well by the electric dipole interaction $p \cdot E$ due to the subwavelength dimensions of the nanorod. Under coherent illumination, this resonance is more pronounced and reaches a peak absorption level of 0.62 at the E-antinode, while it disappears at the E-node. This high level of contrast is achieved because the strength of $p \cdot E$ depends on the magnitude of the E field in the nanorod plane. It should be noted that the absorption enhancement factor of 2.48 observed here is greater than the maximum value of 2 achievable for an ideal, free-standing ultrathin film absorber in a standing wave in free space [24, 25]. This is because in the present case the two input beams are not equal in power due to the lack of directional symmetry.

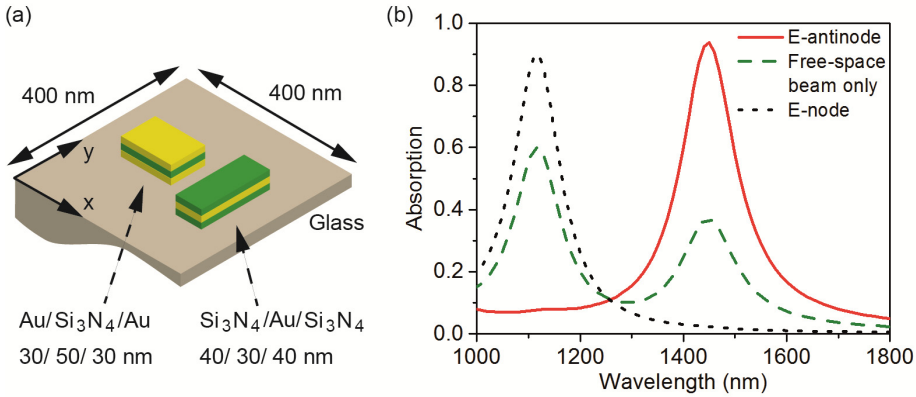

Fig. 3. (a) Schematic of a metamaterial unit cell containing a pair of orthogonally oriented metal-dielectric-metal and dielectric-metal-dielectric nanorods [layer thicknesses as labelled; 280 nm long × 180 nm wide and 270 nm long × 50 nm wide respectively] on an infinitely thick glass substrate. The periodicity of the array is 400 nm in both *x* and *y* directions; The nanorods are separated by a gap of 10 nm. (b) Spectral dispersion of metasurface absorption for coherent illumination modes locating the middle layer of the nanorods at a standing wave E-antinode/B-node [red line] or E-node/B-antinode [black], and for single beam [travelling wave] illumination from the free space side. In all cases, light is polarized in the *y* direction.

Optics EXPRESS

The metamaterial unit cell geometry presented in Fig. 3(a) provides for the demonstration of selective control over both $p \cdot E$ and $m \cdot B$. It contains a pair of resonators - a three-layered Au/Si_3N_4/Au (ASA) nanorod and an orthogonally oriented complementary Si_3N_4/Au/Si_3N_4 (SAS) nanorod. The ASA nanorod has in-plane dimensions of 280 nm × 180 nm, and thicknesses of 30 nm and 50 nm for the Au and Si_3N_4 layers, respectively. The SAS nanorod has in-plane dimensions of 270 nm × 50 nm, and layer thicknesses of 30 nm and 40 nm for the Au and Si_3N_4, respectively. These two nanorods are separated by a gap of 10 nm in the x direction. The refractive index of Si_3N_4 is taken to have a non-dispersive value of 1.8 [26].

Absorption in a single-beam travelling wave from the air side (i.e. the free-space beam only) shows two resonance peaks (Fig. 3(b)). The resonance at 1120 nm comes from the ASA nanorod and can be approximated well by the magnetic dipole interaction $m \cdot B$, which is induced by anti-parallel currents in the two Au layers [27]. The resonance at 1450 nm comes from the SAS nanorod and can be approximated by the electric dipole interaction $p \cdot E$. This resonance is similar to that seen in Fig. 2, as the two Si_3N_4 layers have little influence on the electromagnetic response of the central Au layer. (They are incorporated here for the purposes of maximizing geometric symmetry and minimizing inter-resonator coupling within the unit cell.) By virtue of their different natures, these two resonances can be separately, selectively excited under coherent illumination. Indeed, Fig. 3(b) shows that in the limiting cases of standing wave excitation only one of the two peaks is manifested. The $p \cdot E$ peak is suppressed at the E-node (B-antinode) where $E = 0$, while the $m \cdot B$ peak is suppressed at the B-node (E-antinode) where $B = 0$. As such, coherent illumination can be used as a diagnostic tool for identifying multipolar plasmonic resonances in planar, substrate-supported nanostructures.

4. Thickness measurement for ultrathin films

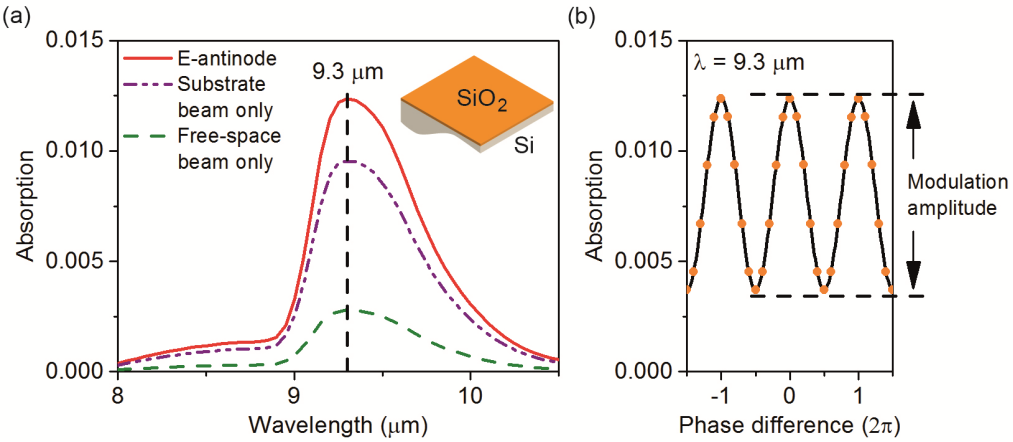

Fig. 4. Detection of ultrathin SiO_2 on Si by coherent illumination spectroscopy: (a) Spectral dispersion of absorption for a 2 nm SiO_2 layer on a semi-infinite Si substrate [as sketched inset] for single beam [travelling wave] illumination from either side and coherent illumination configured to locate the SiO_2 film at a standing wave E-antinode. (b) Magnitude of coherent absorption at a wavelength of 9.3 μm as a function of the relative phase of the two counter-propagating input beams in the SiO_2 layer plane [with relative intensities selected to maximize absorption at zero phase difference, whereby the SiO_2 film is located at a standing wave E-antinode.]. [The spectra in (a) and solid black line in (b) are obtained from finite element numerical simulations; Orange points in (b) are obtained analytically via the scattering matrix method – see Appendix.]

Besides the selective excitation of nanostructural resonances, coherent illumination may be engaged to detect and characterize continuous ultrathin films. Figure 4 illustrates this for the case of a thin layer of SiO_2 on the surface of bulk silicon. We consider a SiO_2 layer with a thickness of 2 nm (approximately the thickness of the native oxidization layer of silicon [28]) with a spectral dispersion of permittivity assumed to be the same as glass, as given in [29].

Optics EXPRESS

The Si substrate is taken to be infinitely thick with a non-dispersive refractive index of 3.42 in the mid-infrared spectral range [29]. At a wavelength of ~9.3 μm the materials have contrasting optical properties, with SiO_2 being absorptive while Si is transparent. Figure 4(a) compares simulated absorption spectra under three modes of illumination, by: (1) a single, travelling light wave impinging from the air (i.e. the free-space beam only); (2) a single beam impinging through the Si substrate (i.e. the substrate beam only); (3) a standing wave formed by two counter-propagating light beams, with the SiO_2 layer at the E-antinode.

Unambiguously detecting, let alone accurately determining the thickness of, such an oxide layer in a single-beam measurement, without an identical but uncoated Si surface for reference, is a challenging proposition: one would need to quantify small (<1%) variations in transmission as a function of wavelength against a large background level, while excluding that they may be due to scattering losses or alignment errors. Layer thickness may be more readily evaluated via measurements of coherent absorption, or more specifically coherent absorption modulation: The maximum level of coherent absorption is achieved, at a wavelength of 9.3 μm, when the SiO_2 layer is located at E-antinode (B-node) of a standing wave, i.e. when the phase difference between two input beams of appropriately balanced intensity is zero (implying that the thin film can be viewed as a planar array of electric dipoles). This level is only slightly higher than the maximum level of single beam absorption (1.24% as compared to 0.96%) but it drops to near zero when the phase difference between the same two input beams is ± π, as shown in Fig. 4(b). (The level of coherent absorption is a sinusoidal function of the input beams' relative phase; it does not drop to zero when they are in antiphase because, without an associated change in relative intensity, this does not locate the SiO_2 layer at an E-node.) (It should be noted here that the same results, for a homogenous thin-film analyte, can be obtained analytically: A scattering matrix derivation is presented in Appendix; analytical and computational results are overlaid in Figs. 4(b) and 5.)

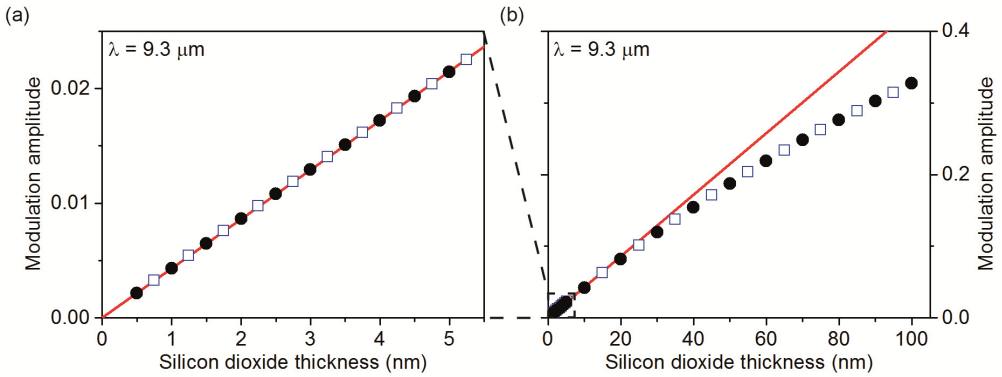

Fig. 5. Evaluating SiO_2-on-Si layer thickness via coherent absorption modulation: Dependence of maximum coherent absorption modulation amplitude on the thickness of SiO_2 calculated for thicknesses (a) up to 5 nm; (b) up to 100 nm, with a straight line fitting to the small thickness range [having a slope of 4.3×10^{-3} nm^{-1}]. Results are presented from both finite element numerical simulations [black dots] and scattering matrix analytical calculations [blue squares].

In an experiment, the phase difference between the two counter-propagating beams in the target plane can be controlled by adjusting either the length of one of the two input beam paths or the position of the sample [8, 9], for example using a piezoelectric delay/translation stage. A periodic variation in one of these parameters would translate to a periodic modulation of coherent absorption, the amplitude of which may be evaluated using phase-locked detection methods. Importantly, while one would still be evaluating absolute variations in absorption (transmission) of order 1%, the coherent measurement is taken against a zero background level (if there is no absorbing layer there is no absorption modulation) and inherently excludes scattering losses (absorption depends on the relative

Optics EXPRESS

phase of the input beams while scattering does not, as discussed in [30]). It may thus provide an accurate measure of SiO_2 film thickness. Coherent absorption modulation amplitude is, to a very good approximation, a linear function of thicknesses up to ~20 nm, with a constant of proportionality equal to 4.3×10^{-3} nm^{-1} (Fig. 5(a)); at greater thicknesses the dependence is seen to be sub-linear (Fig. 5(b)), as would be expected from the dependence of single beam absorption on the thickness of any homogenous medium.

5. Conclusion

In summary, through theoretical analysis and numerical simulation we demonstrate the principle and application potential of coherent illumination spectroscopy for planar nanostructures and homogenous thin (subwavelength thickness) films on bulk, optically thick substrates – a ubiquitous sample configuration in fields ranging from material science, and analytical chemistry to condensed matter physics and nanophotonics/electronics. By controlling the relative phase and intensities of counter-propagating incident beams in the substrate surface plane, standing wave light fields may be configured, for example, to discriminate between the resonant modes of plasmonic nanostructures and to detect absorptive layers even at sub-nanometer thickness. Practical implementation requires only standard interferometric levels of beam alignment and stability, in common with a variety of spectroscopy and metrology techniques. The computational assumption of semi-infinite substrate thickness represents a good approximation to finite, optically thick substrates as long as substrate/air interface reflectivity is low and/or for short pulse illumination.

Data availability

The data from this paper can be obtained from the University of Southampton ePrints research repository: https://doi.org/10.5258/SOTON/D0484.

Appendix: scattering matrix analysis of coherent absorption

Further to the finite element simulation approach described in the main text, coherent absorption in a homogeneous thin film can be evaluated analytically using scattering matrix analysis. The output electric fields E_f' and E_s' are defined in terms of the scattering matrix and the input electric fields E_f and E_s as,

$$\begin{pmatrix} E_f' \\ E_s' \end{pmatrix} = \begin{pmatrix} S_{11} & S_{12} \\ S_{21} & S_{22} \end{pmatrix} \begin{pmatrix} E_f \\ E_s \end{pmatrix} \tag{3}$$

where in the present case E_f and E_f' are light waves in air (i.e. the free-space beams), and E_s and E_s' are light waves in glass or silicon (i.e. the substrate beams). The matrix elements are expressed as,

$$S_{11} = \frac{r_{12} + r_{23} \cdot e^{2i\beta}}{1 + r_{12} \cdot r_{23} \cdot e^{2i\beta}} \tag{4}$$

$$S_{12} = \frac{t_{21} \cdot t_{32} \cdot e^{i\beta}}{1 + r_{21} \cdot r_{32} \cdot e^{2i\beta}} \tag{5}$$

$$S_{21} = \frac{t_{12} \cdot t_{23} \cdot e^{i\beta}}{1 + r_{12} \cdot r_{23} \cdot e^{2i\beta}} \tag{6}$$

$$S_{22} = \frac{r_{32} + r_{21} \cdot e^{2i\beta}}{1 + r_{21} \cdot r_{32} \cdot e^{2i\beta}} \tag{7}$$

Optics EXPRESS

where

$$r_{12} = -r_{21} = \frac{n_1 - n_2}{n_1 + n_2} \tag{8}$$

$$r_{23} = -r_{32} = \frac{n_2 - n_3}{n_2 + n_3} \tag{9}$$

$$t_{12} = \frac{2 \cdot n_1}{n_1 + n_2} \tag{10}$$

$$t_{21} = \frac{2 \cdot n_2}{n_1 + n_2} \tag{11}$$

$$t_{23} = \frac{2 \cdot n_2}{n_2 + n_3} \tag{12}$$

$$t_{32} = \frac{2 \cdot n_3}{n_2 + n_3} \tag{13}$$

$$\beta = \frac{2 \cdot \pi \cdot n_2 \cdot d}{\lambda} \tag{14}$$

The coherent absorption in the thin film is

$$1 - \frac{n_1 \cdot \left|E_f'\right|^2 + n_3 \cdot \left|E_s'\right|^2}{n_1 \cdot \left|E_f\right|^2 + n_3 \cdot \left|E_s\right|^2} \tag{15}$$

The analytical results presented in Figs. 4(b) and 5 are obtained using the following parameters: refractive indices of air $n_1 = 1$, silicon dioxide $n_2 = 2.24 + 2.27i$, and silicon $n_3 = 3.42$; wavelength $\lambda = 9.3$ μm. $d = 2$ nm for Fig. 4(b), and ranges from 0.75 nm to 5.25 nm in steps of 0.5 nm, and from 15 nm to 95 nm in steps of 10 nm for Figs. 5(a) and 5(b) respectively.

Funding

The Royal Society (research grant RG170314); the Engineering and Physical Sciences Research Council, UK (project EP/M009122/1).